The Astrophysical Journal, 879:80 (12pp), 2019 July 10 https://doi.org/10.3847/1538-4357/ab24d6

Testing the Kerr Metric with X-Ray Reflection Spectroscopy of Mrk 335 *Suzaku* Data

Kishalay Choudhury[1], Sourabh Nampalliwar[2], Askar B. Abdikamalov[1], Dimitry Ayzenberg[1], Cosimo Bambi[1,2,5], Thomas Dauser[3], and Javier A. García[4,3,5]

[1] Center for Field Theory and Particle Physics and Department of Physics, Fudan University, 200438 Shanghai, People's Republic of China
[2] Theoretical Astrophysics, Eberhard-Karls Universität Tübingen, D-72076 Tübingen, Germany; bambi@fudan.edu.cn
[3] Remeis Observatory & ECAP, Universität Erlangen-Nürnberg, D-96049 Bamberg, Germany
[4] Cahill Center for Astronomy and Astrophysics, California Institute of Technology, Pasadena, CA 91125, USA
Received 2018 September 20; revised 2019 April 24; accepted 2019 May 25; published 2019 July 9

Abstract

Einstein's gravity has undergone extensive tests in the weak field gravitational limit, with results in agreement with theoretical predictions. There exist theories beyond general relativity (GR) which modify gravity in the strong field regime but agree with GR in the weak field. Astrophysical black holes are believed to be described by the Kerr metric and serve as suitable candidates to test strong gravity with electromagnetic radiation. We perform such a test by fitting one *Suzaku* data set of the narrow-line Seyfert 1 (NLS1) galaxy Mrk 335 with X-ray reflection spectroscopy, using the Johannsen metric to model the black hole spacetime and test for deviations from Kerr. We find the data is best modeled with a hybrid model that includes both partial covering absorption and a reflection component. This is the first time such a model has been proposed for a high-flux (low reflection) Mrk 335 data set. We constrain the Johannsen deformation parameter α_{13} to $-1.5 < \alpha_{13} < 0.6$ with spin parameter $a_* > 0.8$, and the α_{22} parameter to $-0.4 < \alpha_{22} < 2.1$ with $a_* > 0.7$, both at the 99% confidence level. Although additional solutions at large deviations from the Kerr metric show statistical similarity with the ones above, further analysis suggests these solutions may be manifestations of uncertainties beyond our control and do not represent the data. Hence, our results are in agreement with the idea that the supermassive compact object at the center of Mrk 335 is described by the Kerr metric.

Key words: black hole physics – galaxies: active – methods: data analysis – stars: black holes – techniques: imaging spectroscopy – X-rays: individual (Mrk 335)

1. Introduction

Over a hundred years old, Albert Einstein's theory of general relativity has been tested with observations since it was proposed and agreement has been found in numerous cases spanning across a multitude of domains, notably in weak field experiments of the solar system and for radio observations of binary pulsars (Will 2014). Testing gravity in the strong field regime has gained popularity among both the electromagnetic (EM) radiation and the gravitational wave community, with astrophysical black holes proving to be the perfect candidates for carrying out such tests (Yunes & Siemens 2013; Bambi & Nampalliwar 2016; Johannsen 2016; Yagi & Stein 2016; Bambi 2017a; Bambi et al. 2017).

In four-dimensional Einstein gravity, the Kerr metric is the only vacuum black hole solution of the field equations which is regular on and outside the event horizon, under standard assumptions like stationarity and asymptotic flatness, a consequence of the no-hair theorem (Kerr 1963; Carter 1971; Robinson 1975). The general consensus is that the Kerr metric describes the spacetime around astrophysical black holes (Price 1972; Bambi et al. 2009, 2014). But a number of alternative theories predict macroscopic deviations from the Kerr spacetime (Mathur 2005; Dvali & Gomez 2013; Giddings 2014; Berti et al. 2015; Giddings 2017). This makes it imperative to conduct tests on the Kerr hypothesis. Observations of the X-ray reflection spectrum from the black hole neighborhood are particularly interesting, as they can be used to test strong gravity by studying radiation emitted from regions very close to the black hole (Fabian et al. 2000). This method has been developed over the years by assuming the Kerr metric describes the spacetime around the central compact object, in both active galactic nuclei (AGNs) and black hole binaries (BHB). Blurred and distorted emission features can be seen around the reflecting regions of the accretion disk due to relativistic effects, leading to measurements of inner disk radius and black hole spin (Fabian et al. 1989; Laor 1991; Brenneman & Reynolds 2006; Reynolds & Fabian 2008). The most notable and interesting feature is the Fe–Kα emission complex (e.g., Guilbert & Rees 1988; Lightman & White 1988; Fabian et al. 1989; George & Fabian 1991). The utilization of X-ray reflection spectroscopy for strong gravity tests has been examined in the last decade (Schee & Stuchlík 2009; Bambi 2013; Johannsen & Psaltis 2013; Jiang et al. 2015a, 2015b; Bambi et al. 2016; Zhou et al. 2016; Ni et al. 2016; Nampalliwar et al. 2018).

The X-ray blurring code RELXILL is currently the most popular relativistic reflection model in use that describes the reflection spectrum of optically thick, geometrically thin accretion disks (Novikov & Thorne 1973) around black holes (García et al. 2014). The code is the combination of the convoluted (RELCONV) flavor of the RELLINE relativistic smearing model (Dauser et al. 2010, 2013) and the emission-angle-dependent, non-relativistic, local disk reflection code XILLVER (García & Kallman 2010; García et al. 2013). RELCONV was recently modified by some of us to allow for the use of a non-Kerr metric for the purpose of testing gravity (Bambi et al. 2017). Our relativistic blurring code RELXILL_NK has been designed to incorporate any well-behaved, stationary, axisymmetric, and asymptotically flat spacetimes, including parameterized metrics that deform Kerr and solutions in modified gravity theories. Recent results obtained with the

[5] Alexander von Humboldt Fellow.

code for quantifying possible Kerr deviations with X-ray data of multiple sources have been summarized in Bambi et al. (2018). The first non-Kerr metric implemented in RELXILL_NK was the axisymmetric metric proposed in Johannsen (2013). Additional metrics implemented in the framework include the conformal metric of Bambi et al. (2017; see Zhou et al. 2018) and the axisymmetric metric in Konoplya et al. (2016; see Nampalliwar et al. 2019).

The paper is structured as follows. We review the Johannsen metric (expressed in the convention assuming the natural units $G_{\rm N} = c = 1$) in Section 2 for the relativistic blurring code used. Our source is presented in Section 3.1, with the choice of the data set described in Section 3.2. We explain the data reduction methodology in Section 3.3, the listing and briefly explain the model components used for the data analysis in Section 3.4. A justification of the components and key observations leading to our presented results in Section 4 are discussed in Section 5. Finally, we express our concluding remarks and mention possible shortcomings in Section 6.

2. RELXILL_NK: The Metric

One parametrically deformed metric to test the Kerr hypothesis is the Johannsen metric (Johannsen 2013) that we implement in our code RELXILL_NK. Note that the metric is neither a solution of Einstein's field equations nor of any well-motivated modified theory of gravity. We can, however, consider it as a phenomenological hypothesis and conduct strong field tests of the no-hair theorem in general classes of gravity theories.

The line element of the Johannsen metric in Boyer–Lindquist coordinates, with the convention $(-+++)$, is given as

$$\begin{aligned} ds^2 = &-\frac{\tilde{\Sigma}(\Delta - a^2 A_2^2 \sin^2\theta)}{[(r^2+a^2)A_1 - a^2 A_2 \sin^2\theta]^2}\, dt^2 \\ &- \frac{2a[(r^2+a^2)A_1 A_2 - \Delta]\tilde{\Sigma}\sin^2\theta}{[(r^2+a^2)A_1 - a^2 A_2 \sin^2\theta]^2}\, dt d\phi \\ &+ \frac{\tilde{\Sigma}}{\Delta A_5}\, dr^2 + \tilde{\Sigma}\, d\theta^2 \\ &+ \frac{[(r^2+a^2)^2 A_1^2 - a^2\Delta \sin^2\theta]\tilde{\Sigma}\sin^2\theta}{[(r^2+a^2)A_1 - a^2 A_2 \sin^2\theta]^2}\, d\phi^2, \end{aligned} \tag{1}$$

where

$$\begin{aligned} A_1(r) &= 1 + \sum_{n=3}^{\infty} \alpha_{1n}\left(\frac{M}{r}\right)^n \\ A_2(r) &= 1 + \sum_{n=2}^{\infty} \alpha_{2n}\left(\frac{M}{r}\right)^n \\ A_5(r) &= 1 + \sum_{n=2}^{\infty} \alpha_{5n}\left(\frac{M}{r}\right)^n \\ \Delta &\equiv r^2 - 2Mr + a^2 \\ \tilde{\Sigma} &= r^2 + a^2\cos^2\theta + f(r) \\ f(r) &= \sum_{n=3}^{\infty} \epsilon_n\left(\frac{M^n}{r^{n-2}}\right), \end{aligned} \tag{2}$$

with mass M and spin parameter $a = J/M$ of the black hole, where J is the spin angular momentum of the black hole. When the deviation functions $A_1 = A_2 = A_5 = 1$ and $f(r) = 0$, Equation (1) reduces to the Kerr metric. We test for one deformation parameter at a time, keeping all others identically zero. Thus, we present two sets of results, one each for α_{13} and α_{22}. We pick α_{13} and α_{22} because they are expected to have the strongest impact on the reflection spectrum (Bambi et al. 2017), thus their constraints will be the strongest.

Note that there exists a degeneracy between deformation parameters (and among deformation parameters and other model parameters) in terms of their effect on the relativistic blurring, and a systematic study of various kinds of degeneracies is currently underway. But allowing for multiple simultaneous deformation parameters in our reflection model is currently computationally unfeasible owing to memory issues with the analysis package and huge FITS files requirements.

In order to avoid pathologies in the spacetime, the following limits on α_{13} and α_{22} are imposed (Johannsen 2013; Bambi et al. 2017):

$$\alpha_{13} > -\frac{1}{2}(1 + \sqrt{1 - a_*^2})^4 \tag{3}$$

$$-(1 + \sqrt{1 - a_*^2})^2 < \alpha_{22} < \frac{(1 + \sqrt{1 - a_*^2})^4}{a_*^2}, \tag{4}$$

where $a_* = a/M$ is the dimensionless spin parameter present in our code.

3. Data Analysis

3.1. The Source

The narrow-line Seyfert 1 (NLS1) AGN Mrk 335 ($z = 0.0258$) has been found to host a supermassive black hole at its center with reverberation-mapped mass $M \approx 2.6 \times 10^7\, M_\odot$ (Grier et al. 2012). First detected in X-rays by UHURU (Tananbaum et al. 1978), Mrk 335 has been observed and studied numerous times by various X-ray observatories such as *ASCA*, *Swift*, *Suzaku*, *XMM-Newton,* and *NuSTAR* (e.g., Ballantyne et al. 2001; Gondoin et al. 2002; Crummy et al. 2006; Grupe et al. 2007, 2008, 2012; Longinotti et al. 2007; O'Neill et al. 2007; Larsson et al. 2008; Patrick et al. 2011; Gallo et al. 2013, 2015, 2019; Walton et al. 2013; Longinotti et al. 2013; Parker et al. 2014; Wilkins & Gallo 2015; Keek & Ballantyne 2016; Ballantyne 2017; Beheshtipour et al. 2017). It is an extremely variable source, exhibiting more than a factor of 10 fluctuation in the X-ray flux over the past 15 yr. The source has been confirmed to have a Compton reflection component, and a strong soft excess and Fe–Kα line broadening. Distinguishing Mrk 335 data at low energies (<10 keV) between partial absorption and relativistic reflection was a challenge until the first pressing evidence for relativistic reflection from the accretion disk in the AGN was presented by Kara et al. (2013) by studying X-ray reverberation time lags. AGNs exhibit the highest complexity in low-flux states.

3.2. Data

Table 1 presents a list of Mrk 335 data available online for the *Suzaku*, *XMM-Newton,* and *NuSTAR* missions. Mrk 335 was observed in a high-flux state on 2006 June 21 (Obs. ID: 701031010) with *Suzaku* (Mitsuda et al. 2007) for an X-ray Imaging Spectrometer (XIS, Koyama et al. 2007) net exposure time of 151 ks. It is this data set that we will analyze in the present work owing to its limited complexity, good photon counting statistics, and the observation of relativistic reflection

Table 1
Mrk 335 Archived X-Ray Data Studied in the Literature for Select Missions

Instrument	Obs. ID	Date [yyyy/mm/dd]	Exposure Time (ks)
Suzaku	701031010	2006 Jun 21	151.3
	708016010	2013 Jun 11	144.0
	708016020	2013 Jun 14	154.8
XMM-Newton	0101040101	2000 Dec 25	36.9
	0101040701	2000 Dec 25	10.9
	0306870101	2006 Jan 3	133.2
	0510010701	2007 Jul 10	22.6
	0600540601	2009 Jun 11	132.3
	0600540501	2009 Jun 13	82.6
	0741280201	2015 Dec 30	140.4
NuSTAR (FPMA/B)	60001041002	2013 Jun 13	21.3/21.5
	60001041003	2013 Jun 13	21.5/21.3
	60001041005	2013 Jun 25	93.0/92.9
	80001020002	2014 Sep 20	68.9/68.8

in it. The chosen observation uses Walton et al. (2013) as a basis, which is a survey paper investigating relativistic disk reflection for 25 "bare" type 1 AGN *Suzaku* data with little or no complicated intrinsic absorption. The cited work presented findings using the chosen Mrk 335 data set with blurred reflection and showed the presence of relativistically skewed Fe line and a Compton turnover at $E > 10$ keV.

We compare other data in Table 1 against our choice here. Each individual front-illuminated (FI) XIS spectrum (Section 3.3) in our high-flux observation has an effective exposure time (∼133 ks) similar to the total exposure of the *XMM-Newton* high-flux 2006 data set instead, giving us better counts with *Suzaku*. An added detector advantage of *Suzaku* XIS is that it had relatively lower intrinsic background contamination compared to EPIC cameras (Jansen et al. 2001), by construction. Gallo et al. (2013), with a combined ∼200 ks 2009 *XMM-Newton* exposure time, show weak constraints on a_* (similar to Walton et al. 2013) with a deeper analysis of the intermediate-flux data. The remaining data sets (all in low-flux state) have much lower effective exposures and net counts for both satellite missions, in addition to significant warm absorber modification (likely to heighten intercomponent degeneracies) of the reflection data. Flaring in the ∼140 ks 2015 *XMM-Newton* low-flux observations results in a ∼20 ks cutdown, and the remaining observation is photon-starved (Gallo et al. 2019).

It is essential to state that there exist simultaneous high-energy exposures of Mrk 335 with *NuSTAR* (Harrison et al. 2013), which encompasses the full reflection band when used with low-energy satellite data. The only simultaneous observations available as of 2019 April (Table 1) are with the low-flux 2013 Suzaku exposures. Although these *Suzaku* observations amount to ∼300 ks net exposure over ∼7.7 days, there is a threefold issue that builds up problems using these observations. (1) The observations are photon-starved with $<8 \times 10^4$ FI XIS counts (Gallo et al. 2015). (2) The *NuSTAR* coverage is short, corresponds to a very small part of the wide *Suzaku* exposures, and has incredibly low statistics (Parker et al. 2014). (3) A ∼ 90–100 ks flare ∼250 ks in the *Suzaku* observations softens the source spectrum (Wilkins & Gallo 2015), thereby further reducing good intervals for a simultaneous low-flux study, especially creating problems with time-averaged analysis. A simultaneous analysis of Mrk 335 with *NuSTAR*, to date, is not feasible to study strong gravity with reflection spectroscopy owing to a lack of decent coverage.

The struggle with poor detection at the low fluxes with this highly variable source is likely to make it difficult to constrain sensitive parameters such as the deformation parameters. The aim of this work is to study the constraints on possible deviations away from the Kerr metric using data quality with little complexity to avoid complicated intercomponent degeneracies that may shadow our findings. In general, inclusion of other observations may provide more data. But this does not necessarily imply better constraints, since at some point systematic uncertainties dominate over statistical uncertainties (see e.g., Tripathi et al. 2019a; Xu et al. 2018; Zhang et al. 2019).

3.3. Reduction

HEASOFT v6.25 reduction and analysis package was used to process unfiltered event files of the XIS CCDs following the *Suzaku* Data Reduction Guide,[6] using XIS CALDB `v20160607`. Task `aepipeline` was run to create cleaned event files for the FI CCDs XIS0, XIS2 (non-operational since 2006 November), and XIS3. Back-illuminated (BI) CCD XIS1 was not used because its sensitivity is relatively low at Fe K energies. Source (on-center) and background regions of 3.5 arcmin radii were extracted for each FI CCD on the `SAOImage DS9` imaging and data visualization application.[7] Backgrounds were selected from the same CCD by avoiding the source and the ^{55}Fe calibration sources at the corners of the CCD. Unbinned source and background spectra for each CCD were extracted using the XSELECT tool, ensuring the cutoff rigidity was set >6 GeV (Walton et al. 2013) to account for proper non-X-ray background subtraction. The redistribution matrix file (RMF) and the ancillary response file were created using the tools XISRMFGEN and XISARFGEN,[8] respectively. Since we are interested in average spectral properties, the FI CCD spectra and responses were co-added using the FTOOL ADDASCASPEC. The spectra and response files were physically rebinned using the tools RBNPHA and RBNRMF, respectively, with the variable binning scheme shown in the aforementioned guide. On top of this, to reduce bias imposed by a minimum grouping technique (e.g., see Figure 7 in Choudhury et al. 2017) and ensure high signal-to-noise ratio, we grouped our time-averaged XIS data set to 100 cts bin^{-1} using the FTOOL GRPPHA. Apart from data below 0.6 keV and above 10 keV, that between 1.7 and 2.5 keV were also ignored due to uncertainties in detector calibration around Si K edge. The resulting data set had $\approx 5 \times 10^5$ total photon counts between 0.6 and 10 keV with a net count rate of 1.222 ± 0.002 s^{-1} and a very low background contamination (1.2%).

HXD/PIN (Takahashi et al. 2007) data was also reduced similarly: employing `aepipeline` and then the FTOOL HXDPINXBPI using latest CALDB `v20110913`. Evidence of a Compton hump was seen, with a turnover ∼20 keV. However, owing to poor statistics (∼6% of total counts between 0.6–25 keV in PIN) and high errors on the data, in addition to no significant contribution to the analysis of the

[6] https://heasarc.gsfc.nasa.gov/docs/suzaku/analysis/abc/
[7] http://ds9.si.edu/site/Home.html
[8] ftp://legacy.gsfc.nasa.gov/suzaku/doc/xrt/suzakumemo-2011-01.pdf

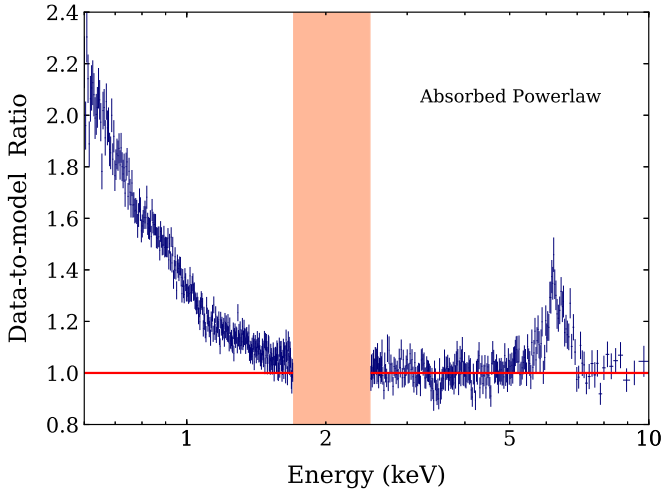

Figure 1. Phenomenological power-law fit to the time-averaged data with $\Gamma \simeq 2.09$. The shaded energy range (1.7–2.5 keV) was not included due to calibration issues. The spectrum was fit from 2.5–4.0 and 8–10 keV, and then plotted after introducing the 0.6–1.7 and 4–8 keV bands, to bring out the Fe and soft band features. The plot was rebinned on XSPEC for clarity.

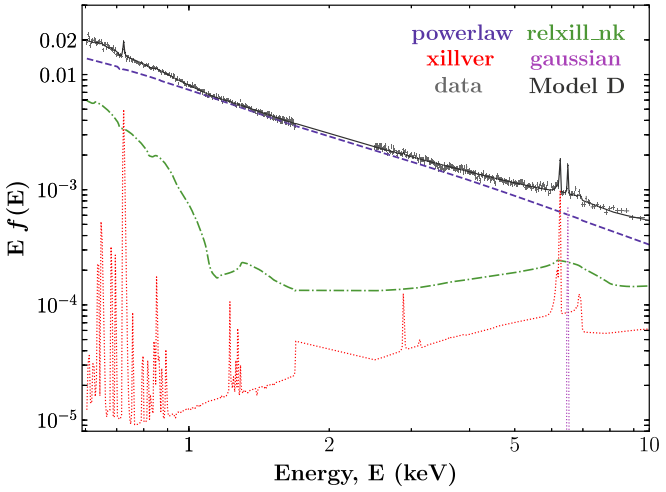

Figure 2. Unfolded spectrum with the best-fit model D. The vertical axis is in units of photons cm^{-2} s^{-1}. Contributions from different model components are shown in different colors.

reflection spectrum, the PIN data set was not included for our test of gravity.

3.4. Modeling

For our work in this paper we made use of the X-ray spectral fitting package XSPEC `v12.10.1b` (Arnaud 1996). The latest (as of 2017 September 4) ionization balance calculation (`v3.0.7`) database was imported additionally to be able to properly account for up-to-date modeling of X-ray emission and absorption from complex spectra.[9]

To bring out features in our 0.6–10 keV spectrum, we first try a phenomenological model—an absorbed power-law fit (Figure 1). The galactic H I column has been fixed to 3.56×10^{20} cm^{-2} (Kalberla et al. 2005) with the ISM grain absorption model TBABS. The cross sections are set by the `abund wilm` command (Wilms et al. 2000). The data show clear signs of a broad Fe K region with a strong soft excess. We ran the fit and obtained poor statistics (χ^2/d.o.f. = 8011.66/971). The 2–10 keV absorbed power-law flux is $\simeq 1.39 \times 10^{-11}$ erg cm^{-2} s^{-1}. Following what we see, we tested out several model combinations on the XIS data set. But we only display results from the physically and statistically relevant models, and explain in Section 5 why others were not favored.

For every combination we start with the possibility that only one deformation (α_{13} or α_{22}) in the Johannsen metric (See Equation (1)) is non-zero, leaving it as a fit parameter and assuming all other deformation parameters are equal to 0. For the sake of avoiding unphysically extreme inner disk inclination fits to a Seyfert 1 AGN (e.g., Nandra et al. 1997; Rakshit et al. 2017), we limit the upper hard limit of the inclination parameter in RELXILL_NK to 75° instead. Tables 2 and 3 display the best-fit parameters obtained for all models with $\alpha_{13} \neq 0$ and $\alpha_{22} \neq 0$, respectively, while Figure 2 shows the unfolded spectrum with the contributions of the additive model components, for our best-fit model.

[9] http://www.atomdb.org/download.php

3.4.1. Model A

TBABS * (ZPOWERLW + RELXILL_NK)

We added our non-Kerr blurred reflection model RELXILL_NK here with the reflection fraction (R_f) parameter fixed at -1, corresponding to a pure reflection signal. The redshifted power-law component (PLC) takes into account the continuum signal separately, with the photon indices Γ linked between the two. Since an $E < 10$ keV data set is not suited for constraining the high-energy cutoff (E_{cut}) in AGN (e.g., refer to Tortosa et al. 2018, for typical values), E_{cut} was fixed at the default value of 300 keV (Keek & Ballantyne 2016). Model A χ^2 plots in Figures 3(a) and (b) show the immense improvement in the fits, with $\Delta\chi^2 > 6800$. Most of the soft excess is accounted for by the blurred reflector (Miller 2007). This suggests the need for a reflection-dominated component (RDC). Still, the convergence is poor and suggests the necessity to consider narrow emission residuals (evident from the χ^2 plots).

3.4.2. Model B

TBABS * (ZPOWERLW + RELXILL_NK + XILLVER)

We made use of the XILLVER reflection code here to account for narrow, non-relativistic reflected emission in the spectrum. From preliminary fits we find that leaving the ionization parameter free here leads to fits of $\log \xi_{unblurred} \approx 0$. Similarly, the fit is insensitive to the value of the inclination parameter of the distant reflector. Hence, we fixed ionization to 0 and inclination to the default. The iron abundance A_{Fe} was linked to that of the blurred reflector with the general idea that the cold reflector could well be part of the same galaxy. Leaving A_{Fe} fixed at solar value returns poor fits. On the other hand, leaving it free results in extremely high, unconstrained abundances at the upper bound. The addition is $>4\sigma$ significant for α_{13} ($\Delta\chi^2 \simeq 26$) and $>5.5\sigma$ significant for α_{22} ($\Delta\chi^2 \simeq 43$), for 1 extra degree of freedom (d.o.f.). Model B χ^2 plots have not been shown because they are very similar to Model C's. (See below.) The middle panel in Figures 3(a) and (b) clearly shows that the narrow Fe core was fit by the model.

Table 2
Best-fit Parameter Values Obtained Employing Models A to D with Only Deformation Parameter $\alpha_{13} \neq 0$

Component	Parameter [Unit]	Model Values[a]			
		A	B	C	D
ZPCFABS	$n_{\rm H}$ [10^{22} cm^{-2}]	...	...	...	$6.57^{+0.88}_{-0.72}$
	CvrFract	...	...	...	$0.24^{+0.03}_{-0.04}$
ZPOWERLW	*PhoIndex*	2.35 ± 0.01	2.35 ± 0.01	2.35 ± 0.01	$2.50^{+0.02}_{-0.03}$
	$norm_1$ [10^{-2} ph cm^{-2} s^{-1} keV^{-1}]	0.80 ± 0.01	0.80 ± 0.01	0.80 ± 0.01	1.09 ± 0.06
RELXILL_NK	q	$7.08^{+0.42}_{-0.36}$	$7.36^{+0.93}_{-0.06}$	$4.11^{+0.39}_{-0.31}$	$10.00^{(P)}_{-4.87}$
	a_*	$0.998^{(P)}_{-0.001}$	$0.998^{(P)}_{-0.001}$	$0.961^{+0.008}_{-0.018}$	$0.990^{+0.007}_{-0.035}$
	i [deg (°)]	$74.2^{(P)}_{-1.5}$	$75.0^{(P)}_{-1.6}$	$55.8^{+0.9}_{-0.3}$	$67.4^{+4.1}_{-3.9}$
	$\log \xi$	$1.23^{+0.08}_{-0.11}$	$1.30^{+0.01}_{-0.14}$	1.25 ± 0.05	$1.29^{+0.03}_{-0.17}$
	$A_{\rm Fe}$	$2.30^{+0.32}_{-0.34}$	$1.61^{+0.44}_{-0.38}$	$1.39^{+0.20}_{-0.40}$	$0.84^{+0.23}_{-0.18}$
	α_{13}	$-0.299^{+0.006}_{-0.025}$	$-0.286^{+0.025}_{-0.018}$	$-1.195^{+0.121}_{-0.256}$	$0.214^{+0.087}_{-1.103}$
	$norm_2$ [10^{-4} ph cm^{-2} s^{-1} keV^{-1}]	3.54 ± 0.17	$3.20^{+0.20}_{-0.26}$	$2.74^{+0.19}_{-0.10}$	$2.87^{+0.22}_{-0.33}$
XILLVER	$norm_3$ [10^{-5} ph cm^{-2} s^{-1} keV^{-1}]	...	$3.33^{+1.10}_{-1.19}$	$3.45^{+0.88}_{-0.86}$	$10.93^{+3.12}_{-2.40}$
ZGAUSS	*LineE* [keV]	...	...	$6.65^{+0.04}_{-0.05}$	$6.66^{+0.03}_{-0.04}$
	flux [10^{-6} ph cm^{-2} s^{-1}]	...	...	$2.99^{+1.40}_{-1.34}$	$4.60^{+1.41}_{-1.37}$
	EW$_{\rm XXV}$ [eV]	...	...	$18.4^{+9.1}_{-9.0}$	$28.5^{+9.2}_{-9.4}$
χ^2/d.o.f.	...	1155.28/964	1128.78/963	1119.02/961	1024.99/959
	...	≈1.198	≈1.172	≈1.164	≈1.069

Note. Errors are given for 90% confidence, unless explicitly stated. A single emissivity profile was adopted (Walton et al. 2013).
[a] "(*P*)" against error values implies the parameter has no bound there.

Table 3
Best-fit Parameter Values Obtained Employing Models A to D with Only Deformation Parameter $\alpha_{22} \neq 0$

Component	Parameter [Unit]	Model Values[a]			
		A	B	C	D
ZPCFABS	$n_{\rm H}$ [10^{22} cm^{-2}]	...	...	...	$6.61^{+0.83}_{-0.72}$
	CvrFract	...	...	...	$0.23^{+0.03}_{-0.02}$
ZPOWERLW	*PhoIndex*	2.36 ± 0.01	2.36 ± 0.01	2.36 ± 0.01	2.50 ± 0.02
	$norm_1$ [10^{-2} ph cm^{-2} s^{-1} keV^{-1}]	0.80 ± 0.01	0.80 ± 0.01	0.80 ± 0.01	$1.09^{+0.06}_{-0.05}$
RELXILL_NK	q	$10.00^{(P)}_{-2.12}$	$10.00^{(P)}_{-0.39}$	$10.00^{(P)}_{-0.47}$	$8.72^{(P)}_{-3.82}$
	a_*	$0.965^{+0.013}_{-0.029}$	$0.977^{+0.016}_{-0.022}$	$0.975^{+0.005}_{-0.016}$	$0.932^{+0.052}_{-0.046}$
	i [deg (°)]	68.2 ± 1.5	$69.9^{+1.45}_{-1.70}$	$70.3^{+0.8}_{-1.7}$	$66.8^{+5.6}_{-4.7}$
	$\log \xi$	$1.24^{+0.06}_{-0.10}$	$1.29^{+0.01}_{-0.15}$	$1.29^{+0.02}_{-0.14}$	$1.29^{+0.03}_{-0.17}$
	$A_{\rm Fe}$	$2.16^{+0.32}_{-0.33}$	$1.45^{+0.41}_{-0.28}$	$1.18^{+0.48}_{-0.19}$	0.83 ± 0.16
	α_{22}	$0.010^{+0.089}_{-0.055}$	$-0.027^{+0.044}_{-0.183}$	$-0.003^{+0.083}_{-0.073}$	$0.311^{+0.811}_{-0.613}$
	$norm_2$ [10^{-4} ph cm^{-2} s^{-1} keV^{-1}]	3.37 ± 0.18	$3.02^{+0.09}_{-0.27}$	$2.89^{+0.18}_{-0.29}$	$2.83^{+0.20}_{-0.31}$
XILLVER	$norm_3$ [10^{-5} ph cm^{-2} s^{-1} keV^{-1}]	...	$4.08^{+1.18}_{-1.11}$	$4.50^{+1.32}_{-1.19}$	$11.01^{+2.20}_{-2.50}$
ZGAUSS	*LineE* [keV]	...	...	6.65 ± 0.04	$6.66^{+0.03}_{-0.04}$
	flux [10^{-6} ph cm^{-2} s^{-1}]	...	...	$2.99^{+1.40}_{-1.37}$	$4.60^{+1.42}_{-1.43}$
	EW$_{\rm XXV}$ [eV]	...	...	18.4 ± 9.0	$28.5^{+9.2}_{-9.1}$
χ^2/d.o.f.	...	1188.04/964	1145.12/963	1133.14/961	1024.90/959
	...	≈1.232	≈1.189	≈1.179	≈1.069

Note. Errors are given for 90% confidence, unless explicitly stated. A single emissivity profile was adopted (Walton et al. 2013).
[a] "(*P*)" against error values implies the parameter has no bound there.

3.4.3. Model C

TBABS * (ZPOWERLW + RELXILL_NK + XILLVER + ZGAUSS)

We detected the presence of a narrow ($\sigma = 10$ eV) Fe-XXV emission line at $E \simeq 6.65$ keV for both α_{13} and α_{22} cases. Existence of this residual was also mentioned in Patrick et al. (2011) and Walton et al. (2013), who analyzed the same data set in Kerr spacetime. The improvement in the delta-fit statistic with the inclusion of such a line in the model agrees with Patrick et al. (2011) (Table 8 therein) at $\Delta\chi^2 \simeq 10$.

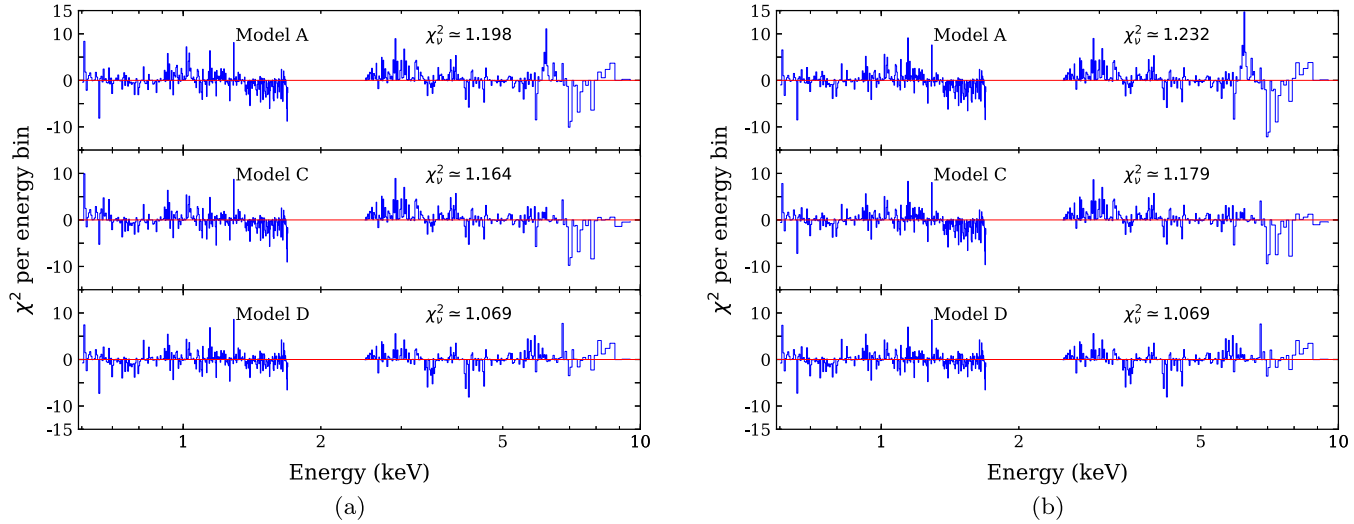

Figure 3. χ^2 plots for models A, C, and D for $\alpha_{13} \neq 0$ (left) and $\alpha_{22} \neq 0$ (right) from Tables 2 and 3, respectively. Plots were rebinned on XSPEC. ν in χ^2_ν represents the degrees of freedom (d.o.f.), where $\chi^2_\nu = \chi^2/\text{d.o.f.}$

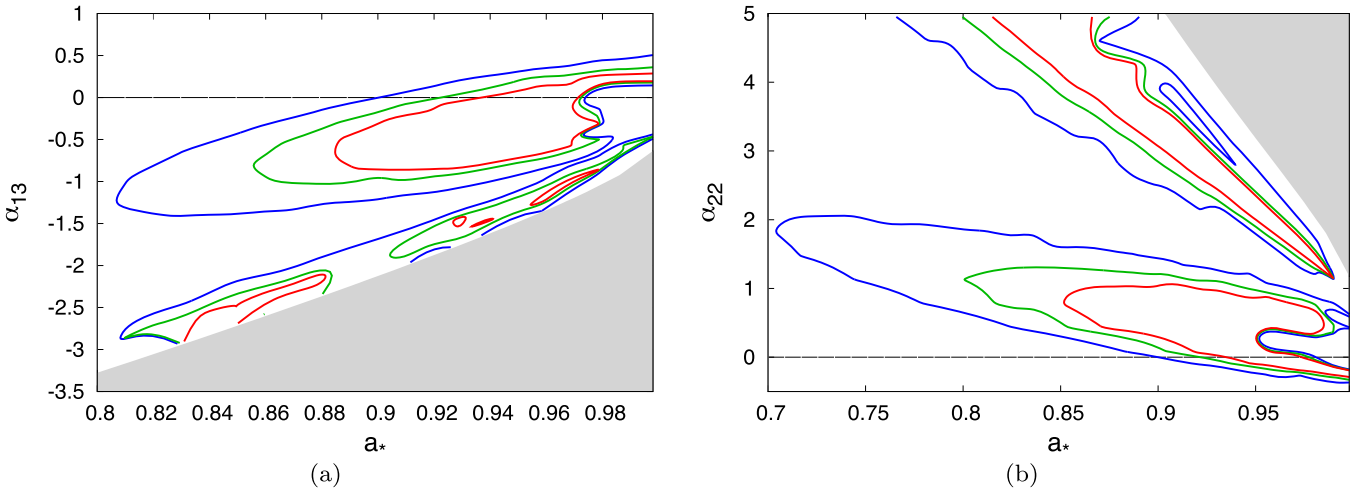

Figure 4. Two-dimensional degeneracy contours between the dimensionless spin parameter a_* and Johannsen deformation parameters α_{13} (left) and α_{22} (right) for the best-fit model D. The dashed horizontal line at 0 marks the Kerr solution. The red, green, and blue contour lines indicate 68%, 90%, and 99% confidence levels, respectively. The shaded spaces in gray are forbidden regions within the metric that avoid some pathological properties as mentioned in Section 2.

3.4.4. Model D

TBABS * [ZPCFABS * (ZPOWERLW + RELXILL_NK + XILLVER + ZGAUSS)]

After Model C, we tried several alternative RDC combinations, briefly described in Section 5. But none of them seemed to improve the fit statistic. However, hints of absorption can be seen in the spectra. We turned to this possibility, and different absorbers and their combinations were examined. The simplest inclusion of one partial covering (ZPCFABS) proved satisfactory. The $\Delta\chi^2$ in the α_{13} and α_{22} cases were, respectively, 94 and 108 for 2 extra d.o.f. The parameters of the covering model are well constrained, as can be seen in Tables 2 and 3. The inclusion improved the fits with high significance ($>7\sigma$). The unfolded spectrum of model D is plotted in Figure 2, along with the contribution of each additive model component.

4. Results

The primary aim of this study is to provide constraints on deviations from the Kerr metric. Tables 2 and 3 list the values of α_{13} and α_{22} for each model. For the best-fit model, model D, the Kerr solution (corresponding to a deformation parameter equal to zero) is recovered in both cases. Because deformation parameters are strongly degenerate with the spin parameter, we show the two-dimensional spin-deformation contours in Figure 4 for α_{13} and α_{22}, using the STEPPAR command on XSPEC. There is a clear degeneracy between the two parameters, which includes the Kerr solution in both cases. Apart from the usual contours observed in such studies (the *near-Kerr* contours; see Figure 2 in Tripathi et al. 2018 and Figure 2 in Xu et al. 2018), additional contours appear that exclude the Kerr solution at 3σ (the *far-Kerr* contours). A thorough investigation (detailed in Appendix A) indicates that

these *far-Kerr* contours are unreliable. We thus ascribe no significance to these. The constraints on the deformation parameters from these plots, after excluding the *far-Kerr* contours, are

$$\begin{aligned} \alpha_{13} \neq 0: \quad & a_* > 0.8 \quad -1.5 < \alpha_{13} < 0.6 \\ \alpha_{22} \neq 0: \quad & a_* > 0.7 \quad -0.4 < \alpha_{22} < 2.1. \end{aligned} \tag{5}$$

We can make some comparisons for α_{13} with constraints from other studies. The constraints obtained here are better than those in Bambi et al. (2018; Figures 2 and 3 therein), which are updated versions of those in Cao et al. (2018) for both 2011 *XMM-Newton* data and simultaneous *NuSTAR*+*Swift* results of the NLS1 1H0707–495. The contours with Markov Chain Monte Carlo (MCMC) runs in Wang-Ji et al. (2018) for the popular X-ray BHB GX 339–4 with *RXTE* PCU-2 data are comparable to ours here. For both deformation parameters, results from Tripathi et al. (2018) on the NLS1 Ark 564 *Suzaku* XIS and from Xu et al. (2018) on the low-mass X-ray binary GS 1354–645 *NuSTAR* FPM analyses are stronger than ours here.

Note that one of the systematic effects that affects the uncertainty in deformation parameter values is the ISCO (innermost stable circular orbit) radius degeneracy between spin and the deformation parameter. (See, e.g., Figure 6 in Johannsen 2013 and Figure 12 in Tripathi et al. 2019b.) Lower spins result in weaker constraints on the deformation parameters. We can see this pattern in all the results. For GX 339–4, the spin is comparable to the spin here, and so is the α_{13} uncertainty; for Ark 564 and GS 1354–645, the spin is higher and is more strongly constrained, so α_{13} also has stronger constraints.

The spin recovered is consistent with the literature where Mrk 335 can be seen to have wide uncertainties on a_* in the Kerr background at 90% confidence for one parameter of interest (e.g., $a_* > 0.7$ in Gallo et al. 2013, with the ∼200 ks *XMM-Newton* intermediate-flux data from 2009). Even Walton et al. (2013) presented a lower limit of 0.7 on a_* with our data set. Our best-fit a_* from Tables 2 and 3 are similar to those from Gallo et al. (2015), who use a broken emissivity profile instead. We roughly recover $0.93 \lesssim a_* \lesssim 0.97$ in the Kerr limit ($\alpha_{13} = \alpha_{22} = 0$) from both Figures 4(a) and (b), at 90% confidence.

5. Discussion

We now discuss some aspects of the models and the results.

5.1. Soft Excess

Absorption in the 1–3 keV band is evident from the absorbed power-law fit, with a strong soft excess <1 keV, both being reported in Keek & Ballantyne (2016). From model fits A to C we see tight parameter constraints, possibly indicating over-estimation of error bars. Comparing with Patrick et al. (2011) and Walton et al. (2013), we observe a rise in Γ and drop in ξ with all four models. This line-continuum trade-off is possible with RELXILL (Choudhury et al. 2017). Recovering a relatively colder disk can also be responsible for causing the soft excess at lower energies, resulting from blending of multiple narrow emission lines that can be fit by blurred reflection (Miller 2007).

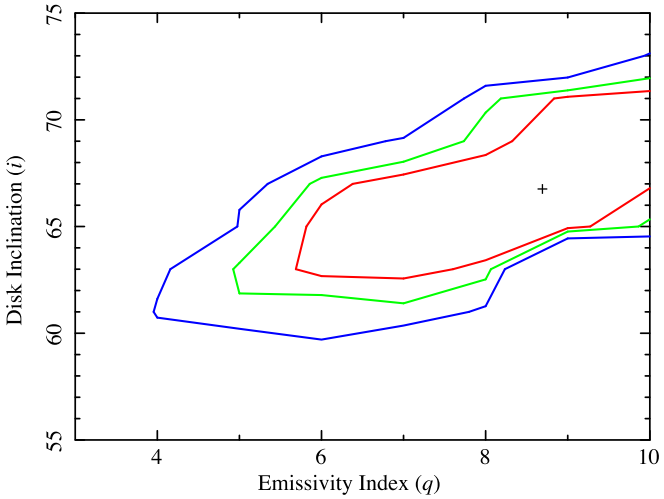

Figure 5. Contour plot between the inner disk inclination i (in units of degrees) and emissivity index q from model D, $\alpha_{22} \neq 0$ case. The red, green, and blue contour lines indicate 68%, 90%, and 99% confidence levels, respectively. The best fit is marked with a "+."

5.2. Inclination Angle

In general, a Seyfert 1 AGN (especially a NLS1) is seen to be more face-on than edge-on, while we obtain a best-fit $i \simeq 67°$. This is comparatively higher than what Walton et al. (2013) report at similar reduced statistics, although we have higher precision. One possible explanation is as follows: the fit values in both Patrick et al. (2011) and Walton et al. (2013) seem to follow the $i - q$ degeneracy trend shown in Parker et al. (2014) (Figure 11 therein) for a time-averaged spectrum analyzed with RELXILL. We also find this degeneracy (see Figure 5) with a preference for $i > 58°$ at 99% confidence. Owing to limited spectral resolution, there could exist a preference for both parameters to yield high fit values in such case. Another possible explanation is that the broad-line region of the AGN is either absent or hidden from the observer, which makes us recover a higher angle (Giannuzzo & Stirpe 1996).

5.3. Absorption

Although Model C here is analogous to the model in Walton et al. (2013, who employ REFLIONX instead; Ross & Fabian 2005), we see that the fits are not satisfactory. We attempted to fit a doubly blurred reflection model (a second RELXILL_NK) with all parameters linked, except for the ionization and normalization (Cao et al. 2018; Tripathi et al. 2018), both with and without the distant reflector. We also inspected with multiple distant reflectors. The inclusions did not improve the fits, implying there may be no accretion disk inhomogeneities as such. A general (or multi-component) PLC +RDC model combination cannot account for this data set with RELXILL_NK. The spectra still had significant residuals beyond 2σ significance at energies <3 keV, which contains ∼80% of the total XIS counts.

To obtain a better fit, we looked at the χ^2 plots. (See model C in Figures 3(a) and (b).) Absorption within the observed (redshifted source) frame $E \sim 7$–8 keV can be seen. Local absorption at the source frame seems possible, as mentioned in Longinotti et al. (2013) and Keek & Ballantyne (2016; see Larsson et al. 2008 and Patrick et al. 2011 for contrary opinions). We decided to add absorbers to the model and found

a better fit. While both ionized and un-ionized absorbers provided better fits, eventually the un-ionized absorber model ZPCFABS was found to be satisfactory. (See Appendix B for details.)

We now discuss the implications of the introduction of such an absorption model in the analysis. Even in the Kerr case, there are results in the literature where we see that a mild continuum absorption of the reflection data improves the fits. Very recent work on the NLS1 Mrk 766 shows that this hybrid scenario is possible and yields more reasonable estimates on the X-ray continuum absorption (Buisson et al. 2018). The referred work finds parameter constraints in line with ours after introducing a partial covering to their reflection model. One of the effects of such absorption is the increase in uncertainty on some or all parameters of interest. We can see such an effect on the estimation of the deformation parameters between Model D and all other models (see, Tables 2 and 3).

Model D, which includes the absorber, gives us a converging best-fit statistic ($\sim$1.07) that is similar to the best-fit model in Walton et al. (2013). Moreover, in Model D both the Fe-XXV line energy and the equivalent width (EW_{XXV}) of the line are similar to that reported in Walton et al. (2013), after possible broadening introduced due to the adjustment offered by the partial covering, reducing the need for narrow emission lines. Additionally, we see in Model D an enhanced signal (rise in the intensity of the distant reflector from $\sim$12% in Model C to $\sim$28% in Model D compared to the total RDC contribution; a rise in Γ by $\sim$6%) as compensation for the flux absorbed, possibly from both the continuum and the cold reflector. At high $i \simeq 67°$, the partial covering barely affects the net model complexity with a Compton-thin continuum absorption under a low $\sim$25% covering, pointing at possible line-of-sight obstruction by local (cold) matter. The net X-ray flux absorbed at the source rest frame from Model C to D is also low ($\Delta L_{0.6-10\,\mathrm{keV}} \simeq (1\text{–}1.5) \times 10^{-2}$ erg s^{-1}).

5.4. Caveats

Our constraints from this work establish that the Kerr metric in Einstein's gravity is recovered at 99% confidence with the data analyzed. However, care needs to be taken while interpreting the results, as there are simplifications involved. The caveats can be divided into four categories:

1. There could exist intercomponent degeneracies, as we include multiple components, and this may add to the wide uncertainties seen in our results. Exempli gratia this is the first time that a partial covering of the reflection spectrum has been proposed for this source in a high-flux data set. Generically, partial absorption and relativistic emission are degenerate with respect to the spectral shape, and a more sophisticated analysis like MCMC is required to check for the robustness of such a combination.
2. The assumption that the intensity profile is a power law is also an approximation. Employing REFLIONX, Gallo et al. (2015) and Wilkins & Gallo (2015) showed that the Mrk 335 corona during the *Suzaku* 2006 observation may have been extended, with a collimated jet-like emission away from the accretion disk up to $\sim$26 gravitational radii (R_g) above the back hole's rotational axis and confined to a small region within a few R_g. They argue that particles were accelerated away from the accretion disk with the base of the unresolved jet possibly moving non-relativistically, and the particles would return under the gravitational effects of the central engine to still sufficiently illuminate the disk with a low ($<$1.0) reflection fraction yield.
3. Even though we have sampled high counts per bin with χ^2-statistics here, we can still be subject to bias in results because our total number of data bins to be fitted (973) is not lower than the squared-root of the total number of counts in the analyzed energy range (Humphrey et al. 2009).
4. The treatment of X-radiation from astrophysical black holes assumes the thin disk model is computationally and physically stable at large, but constitutes typical, over-simplifying assumptions on the disk conditions (Page & Thorne 1974; Bambi 2017b). Taylor & Reynolds (2018) used the lamppost geometry for relativistic reflection spectroscopy using a thick accretion disk. It may be likely that the disk thickens (geometrically) with increasing mass accretion rate. At Eddington luminosity $>$10%, the inner edge of the accretion disk may move further inward than the thin disk approximation where it is thought to be at the ISCO (Abramowicz & Lasota 1980). Keek & Ballantyne (2016) found the analyzed data set here to be on the high end of an accretion rate with an extended corona, which seems to agree with the coronal geometry proposed in Gallo et al. (2015) and Wilkins & Gallo (2015). Work is currently underway to model and test the effects with a thick disk.

6. Conclusions

The main goal of this work is to test how well we can recover the Kerr metric if we introduce a deformation in the Kerr spacetime around the supermassive black hole of NLS1 Mrk 335, using observational data. We use the XSPEC model RELXILL_NK, which is an extension of the widely used relativistic reflection code RELXILL, to include parametrically deformed Kerr metrics. We use the *Suzaku* FI XIS data set, studied in a large survey paper by Walton et al. (2013).

We find differences from the work of Walton et al. (2013). A PLC+RDC model does not explain the data completely and partial covering is needed to account for absorption. We obtain decent constraints on a_*, α_{13}, and α_{22} (shown in Figure 4). At first glance, the results indicate two sets of contours, the *near-Kerr* contours including the Kerr solution and following the results from previous studies, and the *far-Kerr* contours excluding the Kerr solution and including extreme values of deformation parameters. A thorough investigation (see Appendix A) suggests that the *far-Kerr* contours are not robust and sometimes have unreasonable parameter values. Their appearance in the planes of the deformation parameters against a_* and absence with respect to other physical parameters like $\log \xi$ and i with repeated tests indicates there exist uncertainties (possibly data quality and systematics snarled together) currently beyond our control. This is one reason to also say that it is not possible to completely rule out the *far-Kerr* solutions because they exist in at least one two-dimensional parameter phase space. However, except for the spin-deformation contours, all other tests undoubtedly vote in favor of the *near-Kerr* solutions, and thus, our inference in Section 4.

The data analyzed in this study was found to have a best-fit output ∼14%–15% relative strength of relativistic reflection compared to the total contributed by the PLC and the blurred reflector in the RDC.[10] This is the lowest reflection data set of Mrk 335 from Table 1. The proof of this also comes from Wilkins & Gallo (2015), who proposed a change in coronal geometry from the 2006 *XMM-Newton* state to the *Suzaku* state (later the same year), and has become rather extended, beaming more radiation away from the disk in the latter state. The current study, seen from a different perspective, tests for a lower limit using the method of constraining gravity with weak reflection data for Mrk 335. The bounds can only get better from here with a synergy between stronger reflection, better photon counts and appreciable, simultaneous high-energy coverage (see Section 3.2 for a recap on available data and states).

A precision test of gravity using X-ray reflection spectroscopy is a nascent field and every study opens new challenges. Mrk 335 is not an easy source to analyze. The model employed here is the first time RELXILL_NK is combined with a partial covering absorber. The analysis performed here had unique challenges, and the fact that we could obtain constraints comparable to other studies suggests that it is indeed possible to use this technique for testing theories of gravity even in complex scenarios, provided one is careful during the analysis and interpretation of results. The constraints presented in this work are not the strongest (compared to other works in the recent past) owing to the reflection data quality, and certainly do not display the limitations of the X-ray reflection spectroscopy method.

We extend our gratitude to the anonymous referees for suggesting helpful tips in order to improve the quality of the paper. K.C. thanks Michael Parker and Matteo Guainazzi for their helpful comments on the data analysis part. The work of K.C., D.A., A.B.A., and C.B. was supported by the Innovation Program of the Shanghai Municipal Education Commission, grant No. 2019-01-07-00-07-E00035, the National Natural Science Foundation of China (NSFC), grant No. U1531117, and Fudan University, grant No. IDH1512060. K.C. also acknowledges support from the China Scholarship Council (CSC), grant No. 2015GXYD34. S.N. acknowledges support from the Excellence Initiative at Eberhard-Karls Universität Tübingen. A.B.A. also acknowledges the support from the Shanghai Government Scholarship (SGS). C.B. and J.A.G. also acknowledge support from the Alexander von Humboldt Foundation.

Appendix A
The Near-Kerr and Far-Kerr Contours

We now discuss the *near-Kerr* and *far-Kerr* contours of Figure 4. We can see that both panels indicate the presence of multiple minima bound at 99% confidence. While the *near-Kerr* contours remain consistent in shape and size when the stepping resolution (i.e., spacing between two values of a parameter in the grid selected) is changed, the *far-Kerr* contours change significantly with changing resolution. Moreover, often the fits landing in the *far-Kerr* region tend to get stuck, and fail to constrain the deformation parameter

[10] This was determined with the CFLUX model on XSPEC in the 0.6–10 keV band.

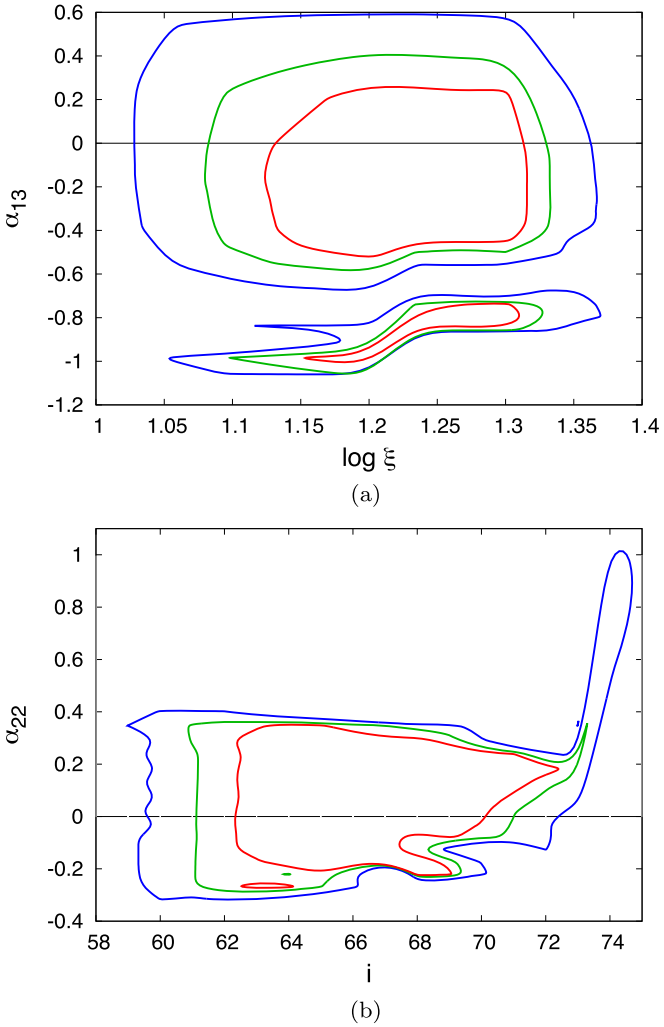

Figure 6. Panel (a): contour plot showing the degeneracy between α_{13} and $\log \xi$ assuming model D. Panel (b): contour plot showing the degeneracy between α_{22} and i assuming model D. The red, green, and blue contour lines indicate 68%, 90%, and 99% confidence levels, respectively.

at both upper and lower bounds. We emphasize at this point that the *near-Kerr* and *far-Kerr* solutions in each panel of Figure 4 are statistically similar (i.e., they have similar $\chi^2/d.o.f.$). Even best-fit values of parameters (other than a_*, α_{13}, and α_{22}) show no systematic difference between fits in the two solution regions. Since the *far-Kerr* feature has never been observed in a similar analysis, we need to check if both *near-Kerr* and *far-Kerr* contours are physically reasonable and robust. Only statistical similarity is not sufficient to reach a conclusion when conducting sensitive tests, like with strong gravity, when a lot of parameters are involved in a complex modeling.

Apart from the fitting glitches (i.e., random fits getting stuck and the failure to yield bounds on the deformation parameters), some additional anomalous behavior were detected when fits would land in the *far-Kerr* minima. In the α_{13} case, for several stepping resolutions, a random fit in the *far-Kerr* minimum showed a drop in the disk temperature ($\log \xi < 1.0$). No other parameter was affected. To investigate further, we calculate the two-dimensional degeneracy between α_{13} and $\log \xi$. Figure 6(a) shows this contour. We

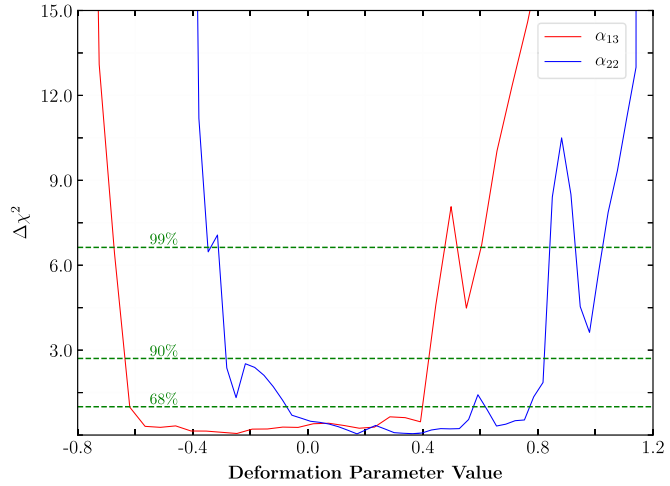

Figure 7. Plot shows the one-dimensional contours of the deformation parameters α_{13} and α_{22} against the delta-fit statistic ($\Delta\chi^2$) with indications for uncertainties at 1 parameter of interest under 68%, 90%, and 99% confidence intervals.

Table 4
Examples of the Limited Domains of Model Parameters for the Final Cross-examination of the *far-Kerr* Solutions

Component	Parameter	Range(s)
ZPCFABS	$n_{\rm H}$	1–1000
		1–100
		2–10
	CvrFract	0.0–0.8
		0.1–0.5
ZPOWERLAW	*PhoIndex*	2.0–2.8
		2.3–2.6
RELXILL_NK	q[a]	4–10
		5–10
		6–10
		1–10
	a_*	0.7–0.998
	i	30–75
		55–75
	$\log\xi$	0.0–3.0
		0.0–2.0
		1.0–2.0
		1.0–4.7
	$A_{\rm Fe}$	0.5–5.0
		0.5–2.0

Notes. All combinations of these sampled ranges were inspected. Parameter units are defined in either Table 2 or 3.
[a] Although Walton et al. (2013) proposed limiting $q \geqslant 3$, we tested with flatter emissivities included and saw that they lead to contours similar to those of Figure 9.

obtain closed contours with $\log\xi > 1.0$ with no hint of extension to lower values, suggesting that the *far-Kerr* minimum with $\log\xi < 1.0$ are outliers. The uncertainty in α_{13} from this plot is much more consistent with the *near-Kerr* contour rather than the *far-Kerr* contour. In the case of α_{22}, random *far-Kerr* fits showed a drop in the inclination values. To investigate further, we compute the two-dimensional $\alpha_{22} - i$ degeneracy. This result is shown in Figure 6(b). Here again we obtain closed contours. The uncertainty in inclination from this plot matches well with that obtained from Figure 5 and the error in α_{22} is consistent with the *near-Kerr* contour rather than the *far-Kerr* contour of Figure 4(b). This again suggests that the *far-Kerr* contours cover a disconnected parameter space and are spurious.

We performed an additional test to check for the robustness of the uncertainty in deformation parameters. Instead of a two-dimensional STEPPAR which shows the degeneracy of a deformation parameter with another model parameter, we perform a one-dimensional STEPPAR with just the deformation parameter. This result is shown in Figure 7. Here we very clearly obtain a contour around the Kerr solution (corresponding to zero deformation parameter) and the range of deformation parameter is consistent with that obtained from the *near-Kerr* contours of Figure 4.

The solutions were further subjected to a final test, by limiting the grids of physical parameters to sensible ranges (Table 4) and checking the results for any difference. We discovered no startling change. The *far-Kerr* solutions do not disappear from Figure 4 nor do they appear in Figure 6.[11] At this point we caution that we do not claim whether the *far-Kerr* solutions are physical or not, but simply describe what this low-reflection data set shows us.

Appendix B
Ionized versus Un-ionized Partial Covering

When applying a partial covering absorber, it was not clear at the onset whether the absorber is ionized or un-ionized. We chose to model the ionized absorber with ZXIPCF and warm absorbers built on XSTAR (Bautista & Kallman 2001). The un-ionized one was modeled with ZPCFABS. With ZXIPCF we did manage to get a better fit over the use of ZPCFABS, where the latter yielded the next-to-best statistical convergence among all model combinations tested with. However, no constraint was obtained for the hydrogen (H I) column $n_{\rm H}$ of the ionized covering against the X-ray continuum index Γ. Among all absorbers, only the ZPCFABS model provided good constraints on $n_{\rm H}$ (see Figure 8), which indicates that the model is statistically restrained. Moreover, it is ZPCFABS that produced decent constraints on both deformation parameters (Figure 4) with comparatively 1 less d.o.f. than ZXIPCF. Figure 9 shows the constraint obtained with Model D if ZXIPCF was used instead. The model completely excludes the Kerr solution. The fit statistic is exceptionally good in this case ($\Delta\chi^2/\text{d.o.f.} = 986.78/958 \sim 1.03$). Naively, one may get mislead by such statistics. But we have seen in other instances, e.g., Xu et al. (2018), that some model degeneracies result in exceptional fit statistics at highly non-Kerr solutions (i.e., excluding the Kerr solution at very large σ), but are usually the result of incorrect modeling. Moreover, we do not obtain any closed contour for the $\alpha_{22} \neq 0$ case with ZXIPCF. We thus conclude in favor of ZPCFABS.

[11] However, $\log\xi$ and i displayed lower uncertainties on the *near-Kerr* deformation parameter bounds, further defying the *far-Kerr* solutions.

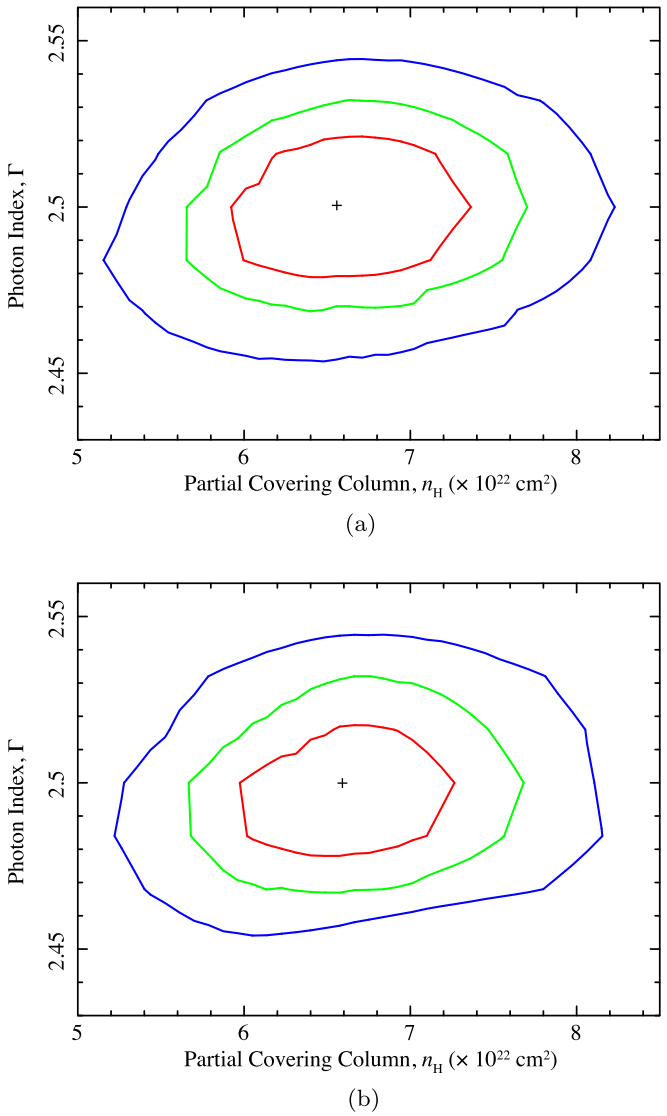

Figure 8. Two-dimensional contour plots showing the degeneracy between the spectral photon index parameter Γ vs. the partial covering hydrogen column n_H in Model D, for $\alpha_{13} \neq 0$ (left) and $\alpha_{22} \neq 0$ (right). Plot was rebinned on XSPEC for clarity.

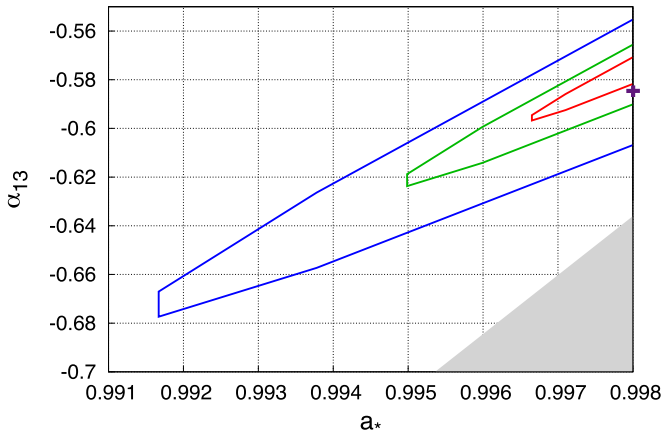

Figure 9. Similar to Figure 4(a), but using ZXIPCF instead of ZPCFABS. The purple "+" marks the best fit. Note that the Kerr solution ($\alpha_{13} = 0$) is not recovered.

ORCID iDs

Cosimo Bambi https://orcid.org/0000-0002-3180-9502

References

Abramowicz, M. A., & Lasota, J. P. 1980, AcA, 30, 35
Arnaud, K. A. 1996, in ASP Conf. Ser. 101, Astronomical Data Analysis Software and Systems V, ed. G. H. Jacoby & J. Barnes (San Francisco, CA: ASP), 17
Ballantyne, D. R. 2017, MNRAS, 472, L60
Ballantyne, D. R., Iwasawa, K., & Fabian, A. C. 2001, MNRAS, 323, 506
Bambi, C. 2013, PhRvD, 87, 023007
Bambi, C. 2017a, RvMP, 89, 025001
Bambi, C. 2017b, Black Holes: A Laboratory for Testing Strong Gravity (Singapore: Springer Nature)
Bambi, C., Dolgov, A. D., & Petrov, A. A. 2009, JCAP, 9, 013
Bambi, C., Jiang, J., & Steiner, J. F. 2016, CQGra, 33, 064001
Bambi, C., Malafarina, D., & Tsukamoto, N. 2014, PhRvD, 89, 127302
Bambi, C., Modesto, L., & Rachwał, L. 2017, JCAP, 1705, 003
Bambi, C., & Nampalliwar, S. 2016, EL, 116, 30006
Bambi, C., Abdikamalov, A., Ayzenberg, D., et al. 2018, Univ, 4, 79
Bambi, C., Cárdenas-Avendaño, A., Dauser, T., García, J. A., & Nampalliwar, S. 2017, ApJ, 842, 76
Bautista, M. A., & Kallman, T. R. 2001, ApJS, 134, 139
Beheshtipour, B., Krawczynski, H., & Malzac, J. 2017, ApJ, 850, 14
Berti, E., Barausse, E., Cardoso, V., et al. 2015, CQGra, 32, 243001
Brenneman, L. W., & Reynolds, C. S. 2006, ApJ, 652, 1028
Buisson, D. J. K., Parker, M. L., Kara, E., et al. 2018, MNRAS, 480, 3689
Cao, Z., Nampalliwar, S., Bambi, C., Dauser, T., & García, J. A. 2018, PhRvL, 120, 051101
Carter, B. 1971, PhRvL, 26, 331
Choudhury, K., García, J. A., Steiner, J. F., & Bambi, C. 2017, ApJ, 851, 57
Crummy, J., Fabian, A. C., Gallo, L., & Ross, R. R. 2006, MNRAS, 365, 1067
Dauser, T., García, J. A., Wilms, J., et al. 2013, MNRAS, 430, 1694
Dauser, T., Wilms, J., Reynolds, C. S., & Brenneman, L. W. 2010, MNRAS, 409, 1534
Dvali, G., & Gomez, C. 2013, ForPh, 61, 742
Fabian, A. C., Iwasawa, K., Reynolds, C. S., & Young, A. J. 2000, PASP, 112, 1145
Fabian, A. C., Rees, M. J., Stella, L., & White, N. E. 1989, MNRAS, 238, 729
Gallo, L. C., Fabian, A. C., Grupe, D., et al. 2013, MNRAS, 428, 1191
Gallo, L. C., Gonzalez, A. G., Waddell, S. G. H., et al. 2019, MNRAS, 484, 4287
Gallo, L. C., Wilkins, D. R., Bonson, K., et al. 2015, MNRAS, 446, 633
García, J., Dauser, T., Lohfink, A., et al. 2014, ApJ, 782, 76
García, J., Dauser, T., Reynolds, C. S., et al. 2013, ApJ, 768, 146
García, J., & Kallman, T. R. 2010, ApJ, 718, 695
George, I. M., & Fabian, A. C. 1991, MNRAS, 249, 352
Giannuzzo, E. M., & Stirpe, G. M. 1996, A&A, 314, 419
Giddings, S. B. 2014, PhRvD, 90, 124033
Giddings, S. B. 2017, NatAs, 1, 0067
Gondoin, P., Orr, A., Lumb, D., & Santos-Lleo, M. 2002, A&A, 388, 74
Grier, C. J., Peterson, B. M., Pogge, R. W., et al. 2012, ApJL, 744, L4
Grupe, D., Komossa, S., & Gallo, L. C. 2007, ApJL, 668, L111
Grupe, D., Komossa, S., Gallo, L. C., et al. 2008, ApJ, 681, 982
Grupe, D., Komossa, S., Gallo, L. C., et al. 2012, ApJS, 199, 28
Guilbert, P. W., & Rees, M. J. 1988, MNRAS, 233, 475
Harrison, F. A., Craig, W. W., Christensen, F. E., et al. 2013, ApJ, 770, 103
Humphrey, P. J., Liu, W., & Buote, D. A. 2009, ApJ, 693, 822
Jansen, F., Lumb, D., Altieri, B., et al. 2001, A&A, 365, L1
Jiang, J., Bambi, C., & Steiner, J. F. 2015a, JCAP, 5, 025
Jiang, J., Bambi, C., & Steiner, J. F. 2015b, ApJ, 811, 130
Johannsen, T. 2013, PhRvD, 88, 044002
Johannsen, T. 2016, CQGra, 33, 124001
Johannsen, T., & Psaltis, D. 2013, ApJ, 773, 57
Kalberla, P. M. W., Burton, W. B., Hartmann, D., et al. 2005, A&A, 440, 775
Kara, E., Fabian, A. C., Cackett, E. M., et al. 2013, MNRAS, 434, 1129
Keek, L., & Ballantyne, D. R. 2016, MNRAS, 456, 2722
Kerr, R. P. 1963, PhRvL, 11, 237
Konoplya, R., Rezzolla, L., & Zhidenko, A. 2016, PhRvD, 93, 064015
Koyama, K., Tsunemi, H., Dotani, T., et al. 2007, PASJ, 59, 23
Laor, A. 1991, ApJ, 376, 90
Larsson, J., Miniutti, G., Fabian, A. C., et al. 2008, MNRAS, 384, 1316
Lightman, A. P., & White, T. R. 1988, ApJ, 335, 57

Longinotti, A. L., Krongold, Y., Kriss, G. A., et al. 2013, ApJ, 766, 104
Longinotti, A. L., Sim, S. A., Nandra, K., & Cappi, M. 2007, MNRAS, 374, 237
Mathur, S. D. 2005, ForPh, 53, 793
Miller, J. M. 2007, ARA&A, 45, 441
Mitsuda, K., Bautz, M., Inoue, H., et al. 2007, PASJ, 59, S1
Nampalliwar, S., Bambi, C., Kokkotas, K. D., & Konoplya, R. A. 2018, PhLB, 781, 626
Nampalliwar, S., Xin, S., Srivastava, S., et al. 2019, arXiv:1903.12119
Nandra, K., George, I. M., Mushotzky, R. F., Turner, T. J., & Yaqoob, T. 1997, ApJ, 477, 602
Ni, Y., Zhou, M., Cárdenas-Avendaño, A., et al. 2016, JCAP, 7, 049
Novikov, I. D., & Thorne, K. S. 1973, in Black Holes (Les Astres Occlus), ed. C. Dewitt & B. S. Dewitt (New York: Gordon and Breach), 343
O'Neill, P. M., Nandra, K., Cappi, M., Longinotti, A. L., & Sim, S. A. 2007, MNRAS, 381, L94
Page, D. N., & Thorne, K. S. 1974, ApJ, 191, 499
Parker, M. L., Wilkins, D. R., Fabian, A. C., et al. 2014, MNRAS, 443, 1723
Patrick, A. R., Reeves, J. N., Porquet, D., et al. 2011, MNRAS, 411, 2353
Price, R. H. 1972, PhRvD, 5, 2419
Rakshit, S., Stalin, C. S., Chand, H., & Zhang, X.-G. 2017, ApJS, 229, 39
Reynolds, C. S., & Fabian, A. C. 2008, ApJ, 675, 1048
Robinson, D. C. 1975, PhRvL, 34, 905
Ross, R. R., & Fabian, A. C. 2005, MNRAS, 358, 211
Schee, J., & Stuchlík, Z. 2009, GReGr, 41, 1795
Takahashi, T., Abe, K., Endo, M., et al. 2007, PASJ, 59, 35
Tananbaum, H., Peters, G., Forman, W., et al. 1978, ApJ, 223, 74
Taylor, C., & Reynolds, C. S. 2018, ApJ, 855, 120
Tortosa, A., Bianchi, S., Marinucci, A., Matt, G., & Petrucci, P. O. 2018, A&A, 614, A37
Tripathi, A., Nampalliwar, S., Abdikamalov, A. B., et al. 2018, PhRvD, 98, 023018
Tripathi, A., Nampalliwar, S., Abdikamalov, A. B., et al. 2019a, ApJ, 875, 56
Tripathi, A., Yan, J., Yang, Y., et al. 2019b, ApJ, 874, 135
Walton, D. J., Nardini, E., Fabian, A. C., Gallo, L. C., & Reis, R. C. 2013, MNRAS, 428, 2901
Wang-Ji, J., Abdikamalov, A. B., Ayzenberg, D., et al. 2018, arXiv:1806.00126
Wilkins, D. R., & Gallo, L. C. 2015, MNRAS, 449, 129
Will, C. M. 2014, LRR, 17, 4
Wilms, J., Allen, A., & McCray, R. 2000, ApJ, 542, 914
Xu, Y., Nampalliwar, S., Abdikamalov, A. B., et al. 2018, ApJ, 865, 134
Yagi, K., & Stein, L. C. 2016, CQGra, 33, 054001
Yunes, N., & Siemens, X. 2013, LRR, 16, 9
Zhang, Y., Abdikamalov, A. B., Ayzenberg, D., et al. 2019, ApJ, 875, 41
Zhou, M., Cardenas-Avendano, A., Bambi, C., Kleihaus, B., & Kunz, J. 2016, PhRvD, 94, 024036
Zhou, M., Cao, Z., Abdikamalov, A., et al. 2018, PhRvD, 98, 024007